Local activation of Cxcl12a signaling controls olfactory placode morphogenesis in zebrafish embryos

Marie Zilliox, Gaëlle Letort, David Sanchez, Christian Rouviere, Pascale Dufourcq, Frédérique Gaits-Iacovoni, Anne Pizzoccaro, Violaine Roussier-Michon, Patrick Blader, Julie Batut

iScience

Article

Local activation of Cxcl12a signaling controls olfactory placode morphogenesis in zebrafish embryos

Graphical abstract

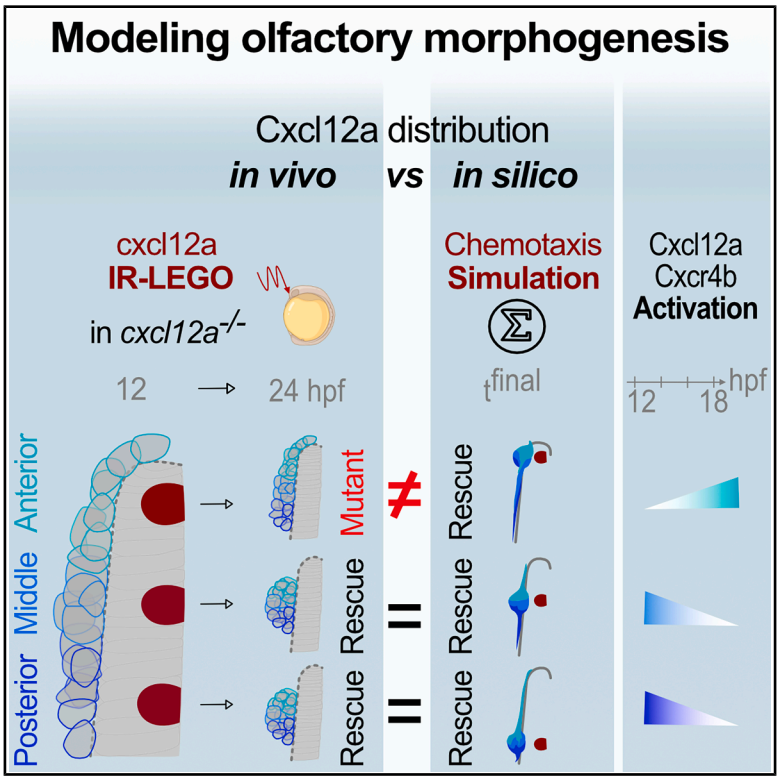

Highlights

- Mathematical model reproduces cxcl12a loss of function in olfactory morphogenesis
- Model-data mismatch reveals spatiotemporal heterogeneity of Cxcl12a signaling
- Local anterior Cxcl12a IR-LEGO activation does not rescue morphogenesis in mutants
- Anterior olfactory placode shows specific Cxcl12a signaling dynamics

Authors

Marie Zilliox, Gaëlle Letort, David Sanchez, ..., Violaine Roussier-Michon, Patrick Blader, Julie Batut

Correspondence

julie.batut@utoulouse.fr

In brief

Biological sciences; Molecular biology; Developmental biology

Zilliox et al., 2025, iScience *28*, 113398
September 19, 2025
https://doi.org/10.1016/j.isci.2025.113398

CellPress

iScience

CellPress
OPEN ACCESS

Article

Local activation of Cxcl12a signaling controls olfactory placode morphogenesis in zebrafish embryos

Marie Zilliox,[1,5,7] Gaëlle Letort,[2,7] David Sanchez,[1,3] Christian Rouviere,[4] Pascale Dufourcq,[1] Frédérique Gaits-Iacovoni,[1] Anne Pizzoccaro,[1] Violaine Roussier-Michon,[3] Patrick Blader,[1,6] and Julie Batut[1,8,*]

[1]Unité de Biologie Moléculaire, Cellulaire et du Développement (MCD, UMR5077), Centre de Biologie Intégrative (CBI, FR 3743), Université de Toulouse, CNRS, UPS, 31062 Toulouse, France

[2]Institut Pasteur, Université de Paris, CNRS UMR3738, Department of Developmental and Stem Cell Biology, 75015 Paris, France

[3]Institut de Mathématiques de Toulouse, UMR5219, Université de Toulouse, CNRS INSA, 31077 Toulouse, France

[4]Image Processing Facility, Center of Integrative Biology, Université de Toulouse, CNRS, UPS, 31062 Toulouse, France

[5]Present address: Institut de Génomique Fonctionnelle de Lyon, Ecole Normale Supérieure de Lyon, CNRS UMR5242, UCBL Lyon-1, 69007 Lyon, France

[6]Present address: Institut de Génétique et de Biologie Moléculaire et Cellulaire (IGBMC), Center National de la Recherche Scientifique (CNRS UMR7104), Institut National de la Sante et de la Recherche Médicale (INSERM U1258), Université de Strasbourg (UNISTRA), 1 Rue Laurent Fries, BP-10142, 67404 Illkirch Graffenstaden, France

[7]These authors contributed equally

[8]Lead contact

*Correspondence: julie.batut@utoulouse.fr

https://doi.org/10.1016/j.isci.2025.113398

SUMMARY

Morphogenesis and cell-type differentiation are highly coordinated in sensory organs to ensure their function. Morphogenesis of the olfactory placode in zebrafish provides a unique model to study this process as undifferentiated cells aligned around the anterior neural plate mature into clusters of early olfactory neurons across a short timescale. Although the Cxcl12a/Cxcr4b signaling pathway drives this process, what constraints on pathway activation apply during morphogenesis are unclear. We developed a mathematical model recapitulating Cxcl12a-mediated olfactory placode morphogenesis. Restoring Cxcl12a expression in mutants for the ligand rescues correct morphogenesis both *in silico* and *in vivo*. However, where expression of the ligand is restored is crucial for rescue, a point not predicted by our model and suggesting an unexpected level of pathway activation control. Analysis of a Cxcr4b activation reporter supports this idea. We concluded that mosaic and heterochronic Cxcl12a activation along the anteroposterior axis sculpts the olfactory placode.

INTRODUCTION

Sensory organs of the vertebrate head permit the detection of an individual's environment. These specialized structures develop early during embryogenesis and are composed largely of neurons and support cells derived from the so-called placodal ectoderm and cranial neural crest.[1] Once formed, each organ displays a specific morphology that is precisely adapted to their distinct function. Each organ is composed of specific sensory cell types that are also tailored to their function, with olfactory neurons being found in the olfactory epithelium of the nose and sensory hair cells found in the inner ear, for instance. Defects in either the morphogenesis of these organs or the correct specification of their sensory cell types can lead to sensory defects such as anosmia or deafness.[2,3]

The zebrafish olfactory epithelium provides a highly tractable system to study the coordinated development of organ form and cell-type diversity. During zebrafish embryo development, olfactory placode (OP) precursors are located at the neural plate border as early as 12 hours postfertilization (hpf) and form a horseshoe around the telencephalon.[1,4,5] This neural border will give rise to the cephalic neural crests and cranial placodes. Cells from the olfactory territory will then assemble into the OP by actively converging and forming two tight clusters on either side of the anterior neural tube between 18 and 21 hpf.[6] Then, a passive lateral movement will give its shape to the cluster starting from 20 hpf.[7] Concomitant to cell convergence, two successive waves of neurogenesis exist, together with three signaling pathways, Cxcl12a/Cxcr4b, Slit/Robo, and Netrin/DCC, which are hierarchically required for axonal guidance of olfactory sensory neurons (OSNs).[4] However, the process of placode formation between 12 and 24 hpf remains poorly characterized. Previous studies have shown that disruption of chemokine signaling through mutations of the chemokine receptor gene *cxcr4b* (*cxcr4b*$^{t26035-/-}$) or its ligand *cxcl12a* (*cxcl12a*$^{t30516-/-}$) leads to defects in the assembly of the OPs, an early step in the

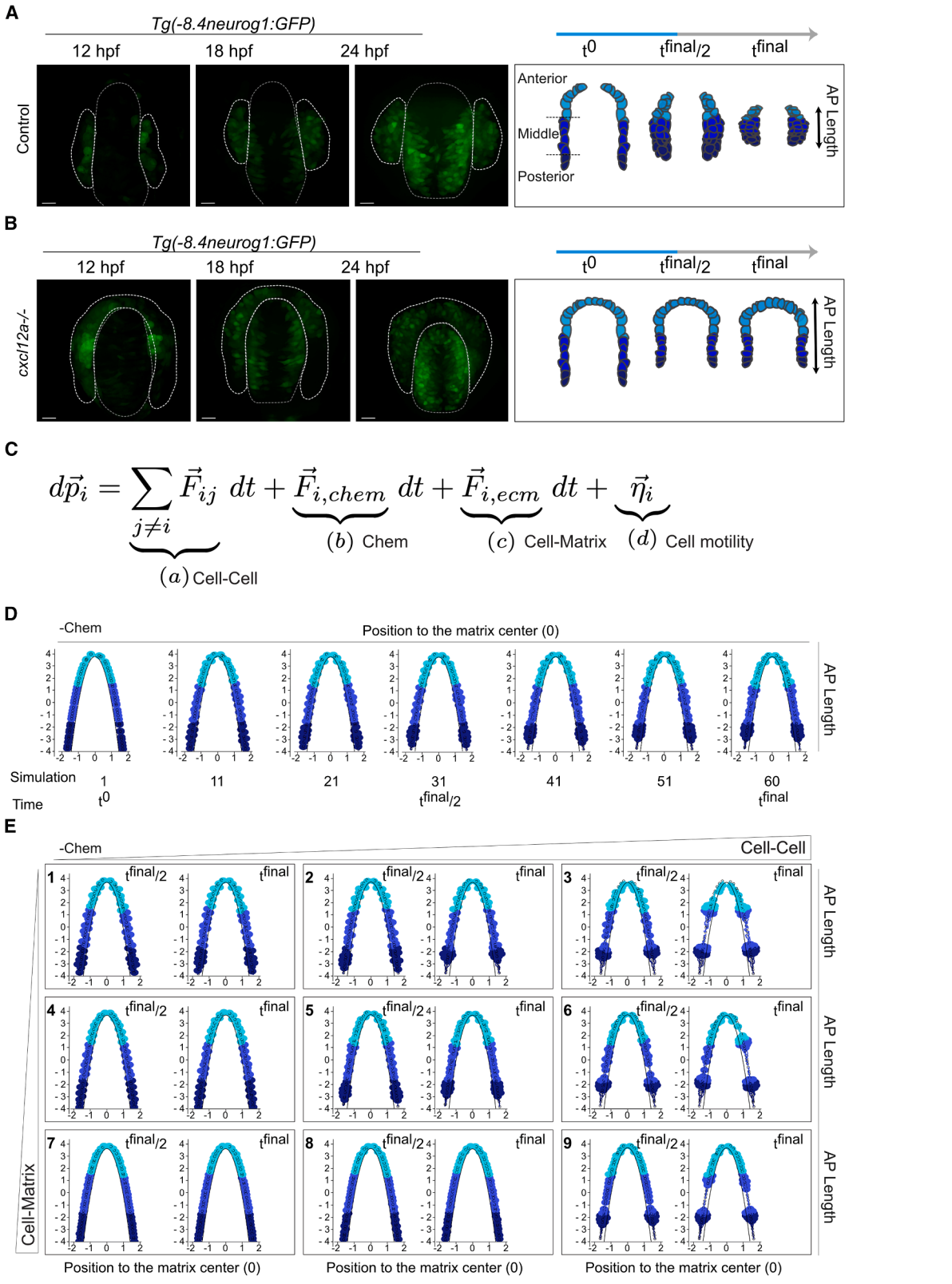

(legend on next page)

development of the olfactory epithelium.[8] Our previous work indicates that two bHLH proneural transcription factors, Neurog1 and Neurod4, share a redundant role in the birth of early olfactory neurons (EONs) and the OSNs during the same developmental time window.[9] Recently, we demonstrated that Cxcr4b is directly regulated by Neurog1.[10] As such, Neurog1 coordinates both morphogenesis and neuronal specification in this system. We know from previous work that *cxcr4b* is expressed by EONs, arranged along the horseshoe, whereas its ligand, *cxcl12a*, is expressed in the adjacent anterior neural plate/tube.[8] How EONs perceive this signal and what parameters control the morphogenesis of the OP are still under debate.

To explore how chemokine signaling controls the convergence of cells to form OPs further, we combined mathematical modeling with *in vivo* experiments; the ability to employ mathematical simulations has become a powerful tool to select and test likely hypotheses concerning developmental mechanisms hidden in the complexity of *in vivo* systems.[11] Using a simple theoretical framework, we tested different distributions of a source of chemotaxis, mirroring the activity of the Cxcl12a/Cxcr4b pathway, and followed if/how they affect the production of a bilateral pair of cell clusters as in the embryo. In parallel, we tested the *in vivo* relevance of similar distributions of Cxcl12a/Cxcr4b pathway activation using infrared (IR) laser-evoked gene operator (IR-LEGO).[12] Interestingly, inducing expression of *cxcl12a* centrally rescues the morphogenesis of the early OP in *cxcl12a* mutant embryos, validating our simulation. Inducing *cxcl12a* expression in an anterior position failed to rescue placode formation, despite our simulations suggesting it should. This discrepancy between *in silico* predictions and *in vivo* observations prompted us to look at the endogenous signaling activity of the Cxcl12a pathway. Our analysis revealed that the chemokine pathway activation dynamics in the anterior compartment is distinct from that in the more posterior regions. Thus, numerical exploration and experimental validation suggest how the distribution of the Cxcl12a signaling drives OP morphogenesis and highlight a spatially controlled dynamics of Cxcr4b activation.

RESULTS

Mathematical model to explore the morphogenesis of the olfactory placode

We developed a mathematical model (Figures 1A and 1C), to test the contribution of chemotaxis, independently of differentiation, during the formation of the OP on either side of the developing forebrain. We chose a center-based framework, considering each cell as a mobile agent characterized by its position and radius. This allowed access to the dynamics of the system and the flexibility to vary the chemotaxis properties. Center-based models have already been determinant in understanding the emergence of collective organization in complex systems, in particular in the context of chemotactic cell migration.[13–18]

In this model, each cell (i) is represented as a circle of constant radius and characterized by its position $p_{i(t)}$ at each time point t. We considered that cell displacement is defined by 4 main forces: interactions with neighbors (a, Cell-Cell, attraction at short distances and hard-core repulsion), chemoattraction (b, Chem, toward the source of a chemoattractant), adhesion to the surface over which it moves (c, Cell-Matrix, short range attraction and hard-core repulsion), and the random motility of an individual cell (d, Cell motility, random motion) (Figure S1A). Considering the system to be at low Reynolds number, we obtained the motion equation for each cell due to the equilibrium of these forces as:

$$d\vec{p}_i = \underbrace{\sum_{j\neq i}\vec{F}_{ij}dt}_{(a)} + \underbrace{\vec{F}_{i,chem}dt}_{(b)} + \underbrace{\vec{F}_{i,ecm}dt}_{(c)} + \underbrace{\vec{\eta}_i}_{(d)}$$

For simplicity, the anterior neural plate was represented as a fixed parabolic, uncrossable barrier for the cells and simulations were performed in 2D with a constant number of cells. The three key stages of olfactory morphogenesis, namely, the olfactory territory at 12 hpf, the OP at 18 hpf, and the olfactory epithelium at 24 hpf, are represented by t^0, $t^{final/2}$, and t^{final} (Figures 1A and 1B). Initially, cells were positioned along the parabolic matrix (20 anterior, 20 middle, and 20 posterior). The python code of the simulations is available on GitHub (https://github.com/gletort/Morphoe), and the specific parameters for each figure are also available (https://github.com/gletort/Morphoe/tree/main and https://github.com/JulieBatut/Zilliox-Letort_2024).

To explore the parameters of the model, we first considered the scenario of an absence of chemotaxis (−Chem in the simulations, Figure 1B). *In vivo*, in the absence of *cxcl12a, Tg(-8.4neurog1:GFP)*-labeled EONs (hereafter referred as olfactory cells) failed to converge correctly along the anteroposterior (AP) axis, with anterior cells remaining anteriorly positioned.[10] Figure 1D shows the output of one simulation every 10 time steps in the absence of chemotaxis (Video S1). In this case, anterior cells (light blue) remained in an anterior position, whereas toward the middle of the simulations, posterior cells (dark blue) migrated slightly anteriorly, reproducing the phenotype described in the absence of *cxcl12a* (Figure 1D, frame 31, $t^{final/2}$; Video S1; and Figures S1B and S1C panel 5). We hypothesized that this behavior of posterior cells was generated by the short-range cell-cell attraction with neighboring cells. Supporting this idea, reducing the strength of adhesion between cells, Cell-Cell (Figure 1E panels 1, 4, and 7 and Videos S2, S5, and S7), decreased the displacement of posterior cells. Increasing

Figure 1. Building a model of olfactory morphogenesis

(A and B) Visualization of olfactory rosette formation in the olfactory placode at 12, 18, and 24 hpf using the *Tg(-8.4neurog1:gfp)*^{sb1} line to label pioneer olfactory neurons in control (A), and *cxcl12a*^{t30516} mutant (B) conditions. A schema of cell position is shown below with anterior cells shown in light blue, middle cells in blue, and posterior cells in dark blue, and the measurement of their size along the anteroposterior (AP) axis is visualized by a black double arrow. Scale bars, 100 μm.

(C) Model equation with the 4 parameters: Cell-Cell interactions (a), Chemotaxis (b), Cell-Matrix interaction (c), and Cell motility (d).

(D) Visualization of the positioning of the cells stained in blue scale according to their positions along the AP axis during a simulation in the absence of chemotaxis (−Chem). All 10 time steps are shown.

(E) Representation of $t^{final/2}$ and t^{final} of a simulation in the absence of chemotaxis (−Chem) as a function of the intensity of the Cell-Cell and Cell-Matrix forces.

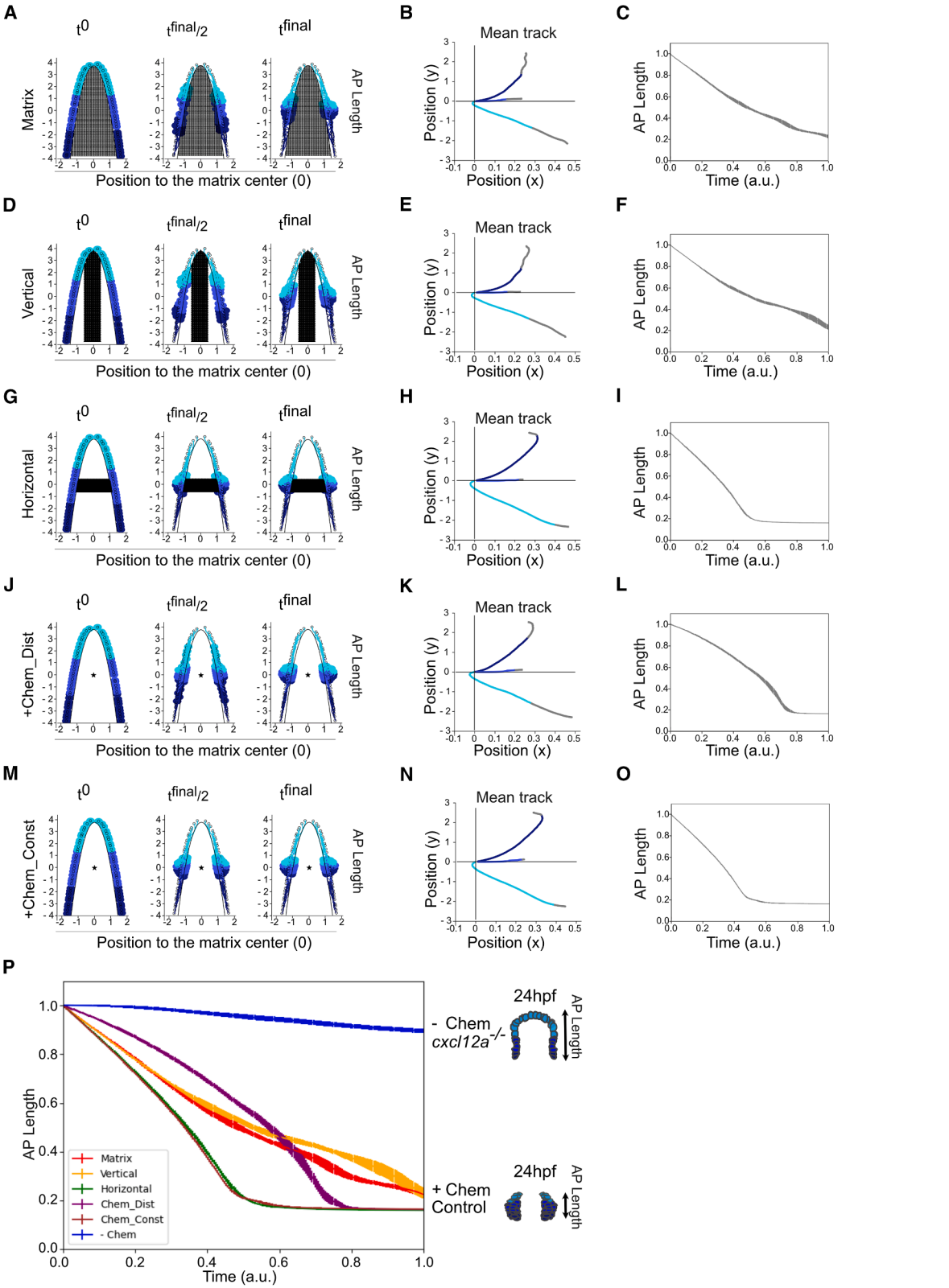

(legend on next page)

Cell-Cell augmented cell compaction leading to the presence of several clusters at the end of simulations (Figure 1E panels 3, 6, and 9 and Videos S4, S6, S9). Varying the adhesion of cells to the telencephalon, Cell-Matrix, had a lower impact than varying Cell-Cell (Figure 1E and Videos S1, S2, S3, S4, S5, S6, S7, S8, and S9) in the range of values tested. At high values, cells tended to remain arrayed along the parabolic surface, which we will hereafter refer to as matrix, maximizing the overall contact, whereas at lower values, Cell-Cell appears to dominate and favors cluster formation. Thus, in the absence of chemotaxis, our model predicts that Cell-Cell interactions are the main motor of cell migration.

In simulations, an intermediate strength of Cell-Cell and Cell-Matrix (Figure 1E panel 5 and Video S1) resulted in a similar distribution of cells to that observed in mutants for *cxcl12a* (Figure 1B). To further look at this similarity, we extracted trajectories of the anterior, middle, and posterior positioned cells over time (compare Figures S1B–S1D with Aguillon et al.[10]). The trajectories of the cells in simulations are color coded from t^0 to $t^{final/2}$ and then represented in black. The average of the 3 positions is also represented to compare the trajectories of cells for each condition (Figure S1C). Another parameter of olfactory morphogenesis at this early stage is the compaction of cells along the AP axis,[7,10,19] which we measured in the simulations as the evolution of their convergence on the *y* axis (which corresponds to the AP axis in the embryo) over time (Figure S1E). All these representations indicate that in the absence of chemotaxis, a balance of Cell-Cell and Cell-Matrix strengths allows the generation of an OP similar to that of a *cxcl12a* mutant *in vivo*.

Effect of the position of *cxcl12a* expression on the morphogenesis of the olfactory placode

Previous studies have shown that *cxcl12a* mRNA is present throughout the anterior neural plate/tube,[8,10] the future telencephalon. Whether this reflects a requirement for such a pattern of chemokine distribution in the correct positioning of the OP at 24 hpf is unclear. To address this, we simulated the outcome of different distributions of the chemotaxis source in the telencephalon by modulating the position of Chem (Figure 2 and Videos S10, S11, S12, S13, and S14). In previous work, the repartition of the guidance molecules has been either explicitly modeled taking into account signal production, degradation, and cell intake,[20] considered as a flat distribution of signal,[21] or following a gradient vanishing away from the source.[22,23] Here, for simplicity, we considered the chemotaxis signal received by each cell as a spatiotemporal constant force directed toward the chemotaxis source, assuming that the cell is sensing a linear chemotaxis gradient.

We compared the results of cell positioning at t^0, $t^{final/2}$, and t^{final} (Figures 2A, 2D, 2J, and 2M), the individual (Figure S2) and average trajectories of 15 simulations of the cells as a function of their position on the AP axis (Figures 2B, 2E, 2H, 2K, and 2N), and the convergence of the cells along the AP axis over the course of the different simulations (Figures 2C, 2F, 2I, 2L, 2O, and 2P). A chemotaxis source filling the whole matrix (Video S10) or in a vertical/medial position (Video S11) generated similar results but did not correspond to the situation seen in wild-type embryos (Figures 2A–2F and 2P, red and yellow lines, respectively; Video S10; and Figure S11) with, for instance, the size of the cell clusters at t^{final} being too large along the AP axis. We did obtain cell clusters similar to those seen in embryos with simulations based on a Chem source in a horizontal position (Horizontal, Figures 2G, 2I, and S2C and Video S12). Similar results were obtained with a centrally located point source of Chem (compared Horizontal and Figures 2G, 2I, and 2J–2O as well as the green and brown plots in Figures 2P, S2C, and S2E and Video S14). Finally, we also tested two scenarios for the evolution of the intensity of the chemotaxis force with a point source: (1) a fixed gradient of intensity (increasing force as cells get closer to the source, +Chem_Dist (Figures 2J–2L and 2P and Video S13) or (2) a constant force (independent of the distance to the source, +Chem_const, Figures 2M–2P and Video S14). A central source with a chemotaxis intensity gradient (+Chem_Dist) showed correct cluster formation (Figures 2J and 2K and Video S13), but not a kinetic evolution of the AP axis length comparable to the control situation in the embryo (Madelaine et al.[9] from which Figure S2F is derived).

In conclusion, simulations with a horizontal source of Chem or a point source and a constant force were sufficient to recapitulate the main outcome of olfactory cluster formation.

Restoring localized source of Cxcl12a rescues the formation of olfactory clusters

According to our simulations, a point source of Chem in the middle of the future telencephalon drives correct assembly of the OP. We tested this *in vivo* by inducing Cxcl12a expression using IR-LEGO[12,24] in *Tg*(*hsp:mcherry-cxcl12a*) transgenic embryos mutant for *cxcl12a*.[25]

Wild-type embryos formed cell clusters that were visualized by the expression of membrane-bound GFP in a *Tg*(*cldnb:lyn-GFP*) background, whereas in *cxcl12a,* mutant clusters adopted an elongated shape along the AP axis (Figure 3A). Measurement of the AP axis of each OP confirmed these results, with an average of 622 ± 25.687 μm against 801.7 ± 19.418 μm per OP, $n = 7$ OP from 4 wild-type embryos and 10 OP from 5 mutant embryos (Figure 3C, compared control in blue and mutant in red). IR-induced expression of Cxcl12a in the center of the

Figure 2. Position of the chemotaxis source controls the compaction of cells along the AP axis to form clusters

(A–O) Result of a simulation at t^0, $t^{final/2}$, and t^{final} when the source is (A, Matrix) positioned throughout the matrix, (D, Vertical) vertical, (G, Horizontal), horizontal, (J, +Chem_Dist) a central fixed gradient, and (M, +Chem_Const) a central constant force with (B, E, H, K, and N) the representation of the average trajectory of the coded cells as a function of their position on the AP axis (light blue, anterior; blue, middle; and dark blue, posterior). The relative size along the AP axis filled by the cells during the simulations is visualized as a function of the source position (C, F, I, L, and O).

(P) Representation of the set of relative sizes along the AP axis occupied by the cells step by step. The curves are colored according to the position of the source (Matrix = red, Vertical = yellow, Horizontal = green, Central source Chem_Dist = purple, central source Chem_Const = brown, and without chemotaxis, −Chem = blue).

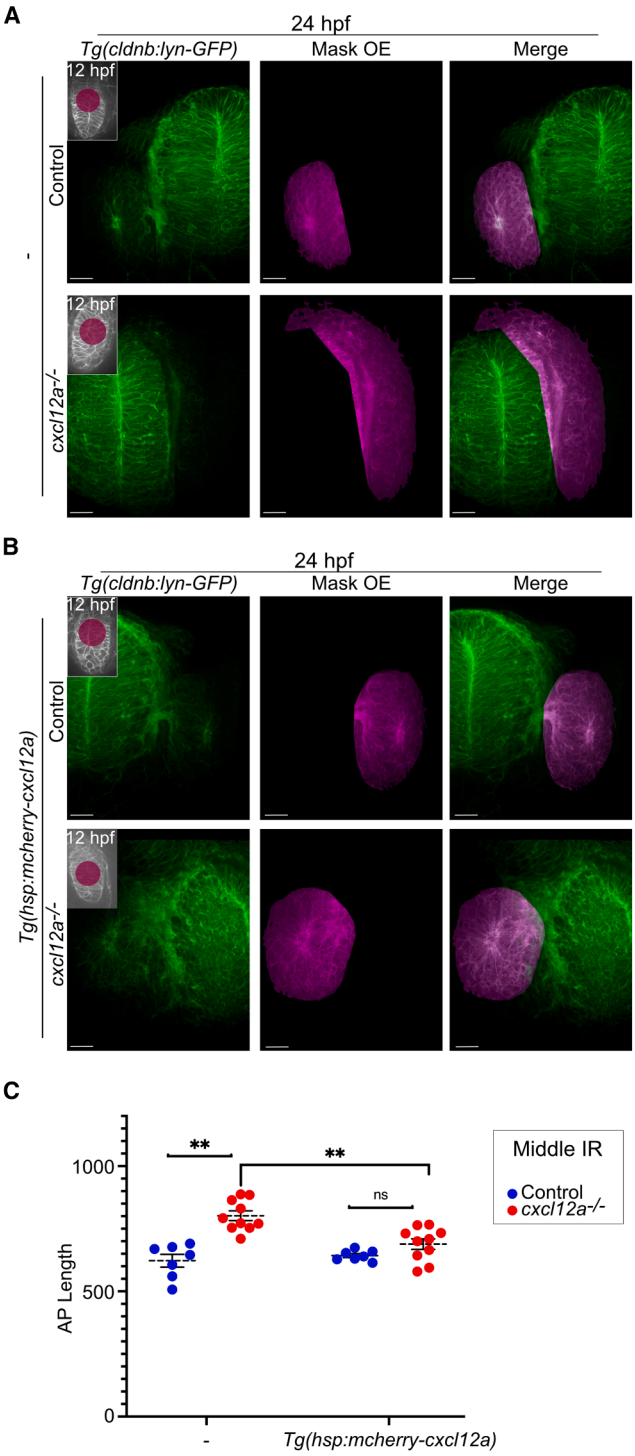

Figure 3. Expression in the middle of the forebrain of *cxcl12a* can rescue olfactory rosette formation in *cxcl12a*^{t30516} mutant

(A and B) OP assembly visualized at 24 hpf using the *Tg*(*cldnb:lyn-GFP*) transgenic line in control and *cxcl12a* mutant (*cxcl12a*$^{-/-}$) embryos under (A, –) control or (B, *Tg*(*hsp:mcherry-cxcl12a*)) conditions in the presence of central *cxcl12a* expression. Rosettes are visualized using the Imaris surface tool and represented by a mask OE. A merge of the *Tg*(*cldnb:lyn-GFP*) line and the mask is shown. The embryo is shown with anterior up. Scale bars, 100 μm.

anterior neural plate at 12 hpf (Figures 3B and 3C, *Tg*(*hsp:mcherry-cxcl12a*)) did not affect the AP length of clusters at 24 hpf in the wild-type conditions (642.429 ± 7.816 μm, n = 7 OP, Figures 3B and 3C, blue); expression was visualized via mCherry fluorescence (Figure S3). In *cxcl12a* mutant embryos, induced expression of Cxcl12a restored a cluster size comparable to the control situation (688.400 ± 20.973 μm, n = 10 OP, Figures 3B and 3C, red). Altogether, these data strengthened the predictive capacity of our mathematical model. On the other hand, they open the question of the pertinence of the broad transcription of *cxcl12a* in the presumptive telencephalon, as this configuration of Chem does not produce wild-type convergence of olfactory cell clusters in our simulations.

Clustering of cells along the AP axis is sensitive to the position of a point source of Cxcl12a expression

We further challenged our model by testing cluster formation after induction of Chem/Cxcl12a expression at different positions both in simulations (*in silico*) and embryos (*in vivo*) in -Chem or *cxcl12a* mutant embryos, respectively.

Simulations based on a posterior source led to the formation of two clusters in a posterior position with a normal AP axis length (Figures 4A–4C and S4A and Video S15). The results of an IR-induced posterior Cxcl12a expression in *cxcl12a* mutant embryos look similar to the results of the simulation (Figures 4D, 4E, and 4K) with formation of two clusters and an average AP length of 570 ± 45.806 μm (IR-induced Chem), n = 4 OP, compared with 794.5 ± 30.633 μm (non-induced Chem), n = 4 OP in *cxcl12a* mutants (without Chem); in the wild-type embryos, the averages were comparable without or with IR-induced Chem with, respectively, 505 ± 35.081 μm, n = 4, and 570 ± 45.806 μm, n = 4. Again, the induction of Cxcl12a expression could be visualized specifically by mCherry expression (Figures S4B, S4C, S5B, and S5C). Simulations based on anterior Chem resulted in the formation of two clusters in an anterior position or merged clusters across the anterior midline but with clustering kinetics along the AP axis comparable to the control situation (Figures 4F–4H and S5A and Video S16). In contrast, in *cxcl12a* mutant embryos, anterior expression of Cxcl12a did not rescue the mutant phenotype (Figures 4I, 4J, and 4L). After IR induction, clusters displayed an average AP axis length of 822.500 ± 19.103 μm, n = 14 OP, whereas without induction, the average AP axis was 705.214 ± 30.638 μm, n = 14 OP; AP axis length in control embryo was 525.500 ± 7.853 μm, n = 14 OP, and

(C) Measurement of the length of the AP axis occupied by cells at 24 hpf from the area occupied by *Tg*(*cldnb:lyn-GFP*) in control (Control, blue) or *cxcl12a* mutant (*cxcl12a*$^{-/-}$, red) conditions. A significant difference is observed between control and mutant embryos in the control condition (–, without exogenous *cxcl12a* expression), $^{**}p$ = 0.0016 (mean OP size is 622 ± 25.687 μm vs 801.7 ± 19.418 μm, n = 7 and 10, respectively). Conversely, when *cxcl12a* is expressed centrally (*Tg*(*hsp:mcherry-cxcl12a*)), there is no difference between control and mutant, ^{ns}p = 0.1872 (mean OP size is 642.429 ± 7.816 μm vs 688.400 ± 20.973 μm epithelium, n = 7 and 10, respectively). However, there is a difference between the size along the AP axis of the OP of mutant embryos in the absence and presence of exogenous *cxcl12a* expression, $^{**}p$ = 0.0070 (801.7 ± 19.418 μm vs 688.400 ± 20.973 μm OP, n = 10). Shown are mean ± SEM. p Values are calculated using a paired t test; ns, not significant.

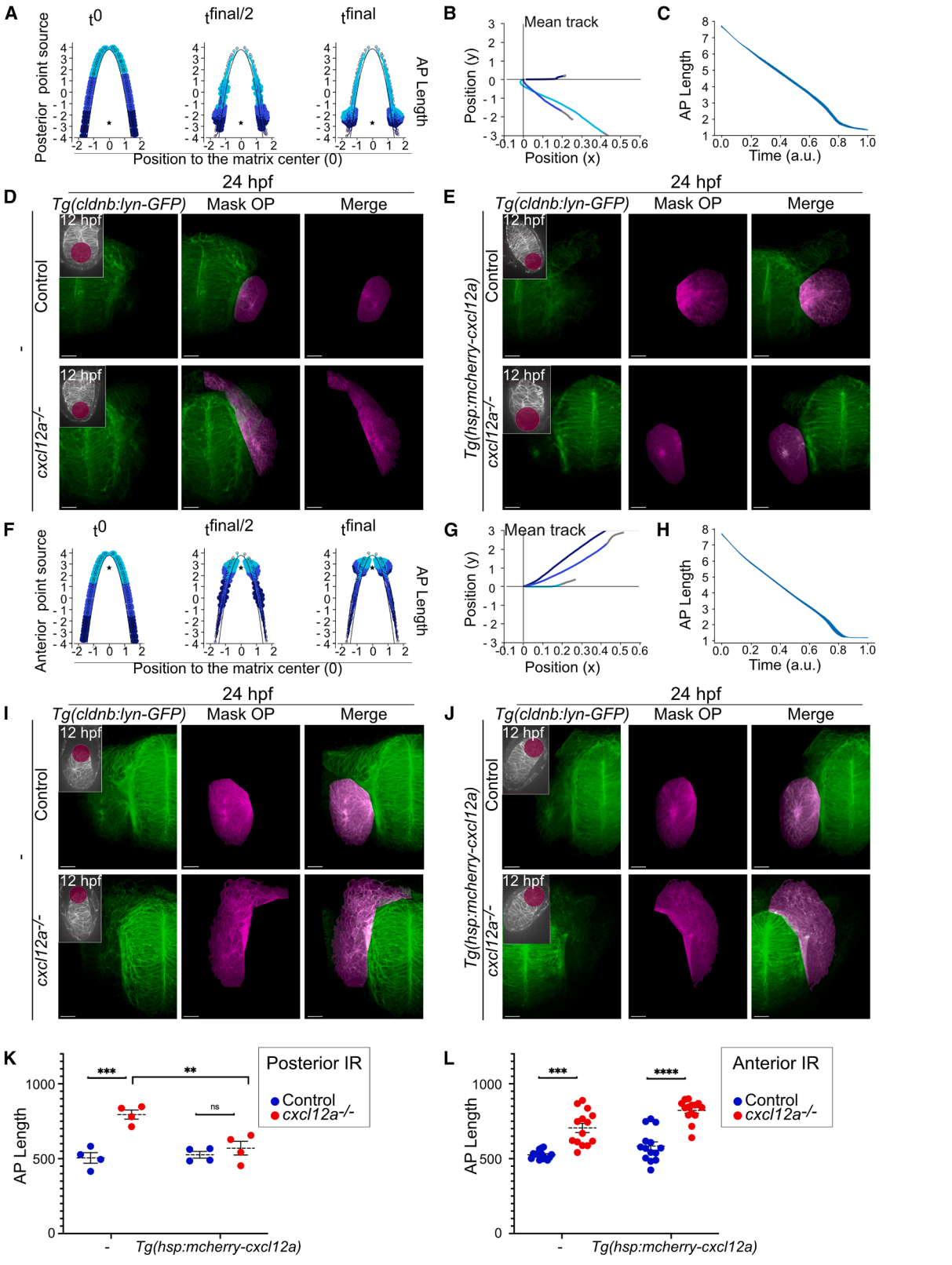

(legend on next page)

584.357 ± 27.963 μm, n = 14 OP, in the absence or presence of induced Cxcl12a expression, respectively (Figure 4L).

From these results, we conclude that our model faithfully predicts the behavior of inducing central and posterior expression of Cxcl12a in the absence of Chem. Conversely, whereas an anterior point source of Chem generated 2 anterior clusters in the model, IR-LEGO Cxcl12a induced anteriorly has no effect in the mutant. This discrepancy between *in silico* and *in vivo* observations challenged our simplistic assumptions, suggesting that activation of the chemokine pathway downstream of the ligand is modulated along the AP axis.

The anterior part of the olfactory placode shows specific Cxcl12a signaling dynamics

To understand the differences in the predictive power of our model along the AP axis, we analyzed the dynamics of activation of the Cxcl12a pathway in embryos using the previously developed *Tg*(*cxcr4b-mKate2-IRES-EGFP-CAAX*) transgenic reporter of Cxcl12a signaling[26] (Figure S6A, and https://github.com/JulieBatut/Zilliox-Letort_2024/tree/main/Figure5). In this reporter line, activation of the pathway leads to the internalization of Cxcr4b and the appearance of mKate2 puncta in the cytoplasm of cells with EGFP-CAAX+ membranes (blue arrowheads in Figures 5A, 5B, and S6). To analyze imaging data, we developed a Java Fiji[27] macro (see materials and methods) to quantify the number of mKate2 puncta in cells with EGFP-CAAX membranes using Cellpose-based segmentation.[28] Our results indicate that the dynamics of cell numbers visualized with this transgene are similar in the posterior and middle compartments, increasing from 12 to 18 hpf before decreasing slightly at 24 hpf (Figure S7A). Indeed, the dynamics of pathway activity (i.e., the number of cells) in the middle compartment doubled from 12 to 18 hpf, rising from 73 (±11, n = 4) at 12 hpf to 88 (±10, n = 6) at 14 hpf, 116 (±10, n = 6) at 16 hpf, 156 (±22, n = 4) at 18 hpf, and 117 (±22, n = 4) at 24 hpf. Conversely, during the same time window the number of cells in the anterior compartment displaying pathway activity decreased by 2-fold, from 45 (±5, n = 4) at 12 hpf to 41 (±6, n = 6) at 14 hpf, 45 (±7, n = 6) at 16 hpf, and 28 (±4, n = 4) at 18 hpf, followed by a rebound to 60 (±14, n = 4) at 24 hpf suggesting oscillatory behavior.

Interestingly, we found similar trends when we quantified the number of cells that have Cxcr4b at their membrane but without intracellular spots suggesting that they do not activate the signaling pathway (competent cell, Figure S7B). The number of competent cells in the middle compartment almost tripled from 30 (±9, n = 4) at 12 hpf to 57 (±9, n = 6) at 14 hpf, to 63 (±11, n = 6) at 16 hpf, and to 88 (±13, n = 4) at 18 hpf. Again, this number seems to oscillate in the anterior compartment, from 18 (±4, n = 4) at 12 hpf to 24 (±5, n = 6) at 14 hpf, to 26 (±7, n = 6) at 16 hpf, and to 10 (±3, n = 4) at 18 hpf (Figure S7B).

We then used two indicators of the presence of Cxcl12a by quantifying the number of intracellular Cxcr4b+ points in cells expressing Cxcr4b. Category 1 spots correspond to the number of cells with 1–5 intracellular spots, whereas Category 2 corresponds to the number of cells with more than 6 intracellular spots relative to the total number of cells. In contrast to the number of competent cells over the same period (i.e., 12–18 hpf), the proportion of cells containing between 1 and 5 spots per cell (Cat 1 Spot) remained stable in the anterior cells, whereas it decreased in the other compartments (Figure 5C). A different trend was observed for cells with 6 or more Cxcr4b+ spots (Figure S7C, Cat 2 Spot), with the anterior and posterior domains appearing to behave in the same way (decrease with a peak at 16 hpf and regrowth to reach or exceed the initial level at 12 hpf) and the middle domain describing a bell curve with a peak also at 16 hpf (Figure S7C, Cat 2 Spot). We next determined a Cxcl12a signaling activation score (Figure 5D) by quantifying the number of total Cxcr4b+ spots over the number of cells expressing Cxcr4b (EGFP-CAAX+). Interestingly, cells from the anterior compartment had an overall higher score than the other compartments, rising from 1.2 (±0.13, n = 4) at 12 hpf to 2.5 (±0.43 n = 4) at 18 hpf, whereas decreasing from 0.9 (±0.07, n = 4) at 12 hpf to 0.48 (±0.04, n = 4) at 18 hpf for cells in the middle compartment and decreasing from 2.3 (±0.26, n = 4) at 12 hpf

Figure 4. Model and embryo testing of posterior and anterior *cxcl12a* expression on morphogenesis of the olfactory placode

(A and F) Simulation of olfactory placode assembly at t^0, $t^{final/2}$, and t^{final} in the presence of a (A) posterior or (F) anterior source.

(B and G) Average cell trajectory as a function of cell location. Anterior in light blue, middle in blue, and posterior in dark blue.

(C and H) Time course of the length occupied by the cells along the AP axis.

(D and E) Olfactory placode (OP) formation visualized at 24 hpf using the *Tg*(*cldnb:lyn-GFP*) transgenic line in control and *cxcl12a* mutant (*cxcl12a*$^{-/-}$) embryos under control (D, −) or (E, *Tg*(*hsp:mcherry-cxcl12a*)) conditions with or without Tg(*hsp:mcherry-cxcl12a*). Rosettes are visualized using the Imaris surface tool and represented by an OP mask. A merge of the *Tg*(*cldnb:lyn-GFP*) line and the mask is shown. The embryo is shown with the anterior up. Scale bars, 100 μm.

(I and J) Olfactory placode (OP) formation visualized at 24 hpf using the *Tg*(*cldnb:lyn-GFP*) transgenic line in controls and *cxcl12a* mutants (*cxcl12a*$^{-/-}$) embryos under control (I, −) or (J, *Tg(hsp:mcherry-cxcl12a)*) conditions in the presence of anterior *cxcl12a* expression. Rosettes are visualized using the Imaris surface tool and represented by an OP mask. A fusion of the *Tg*(*cldnb:lyn-GFP*) line and the mask is shown. The embryo is shown with the anterior up. Scale bars, 100 μm.

(K) Measurement of the length of the AP axis occupied by cells at 24 hpf from the area occupied by *Tg*(*cldnb:lyn-GFP*) in controls (Control, blue) or *cxcl12a* mutants (*cxcl12a*$^{-/-}$, red) when *cxcl12a* is expressed in the posterior. A significant difference is observed between control and mutant embryos in the control condition (−, without exogenous *cxcl12a* expression), ***p = 0.0009 (mean OP size is 505 ± 35.081 μm vs 794.5 ± 30.633 μm, n = 4 and 4, respectively). Conversely, when *cxcl12a* is expressed posteriorly (*Tg*(*hsp:mcherry-cxcl12a*)), there is no difference between control and mutant, ^{ns}p = 0.4328 (mean OP size is 526 ± 22.275 μm vs 570 ± 45.806 μm, n = 4 and 4, respectively). However, there is a difference between the size along the AP axis of the OP of mutant embryos in the absence or presence of *cxcl12a* expression, **p = 0.0087 (794.5 ± 30.623 μm vs 570 ± 45.806 μm, n = 4 and 4, respectively). There is no difference if you compare control conditions without or with *cxcl12a* expression, ^{ns}p = 0.6345 (505 ± 35.081 μm vs 526 ± 22.275 μm, respectively).

(L) Measurement of the length of the AP axis occupied by cells at 24 hpf from the area occupied by *Tg*(cldnb:lyn-GFP) in controls (control, blue) or *cxcl12a* mutant (*cxcl12a*$^{-/-}$, red) when *cxcl12a* is expressed in the anterior. A significant difference is observed between control and mutant embryos in the control condition (−, without exogenous *cxcl12a* expression), ****$p < 0.0001$ (mean OP size is 525.500 ± 7.853 μm vs 705.214 ± 30.638 μm, n = 14 and 14, respectively). Conversely, when *cxcl12a* is expressed anteriorly (*Tg*(*hsp:mcherry-cxcl12a*)), there is a significant difference between control and mutant, ****$p < 0.0001$ (mean OP size is 584.357 μm ± 27.963 vs 822.500 ± 19.103 μm, n = 14 and 14, respectively). Shown are mean ± SEM. p Values are calculated using a paired t test.

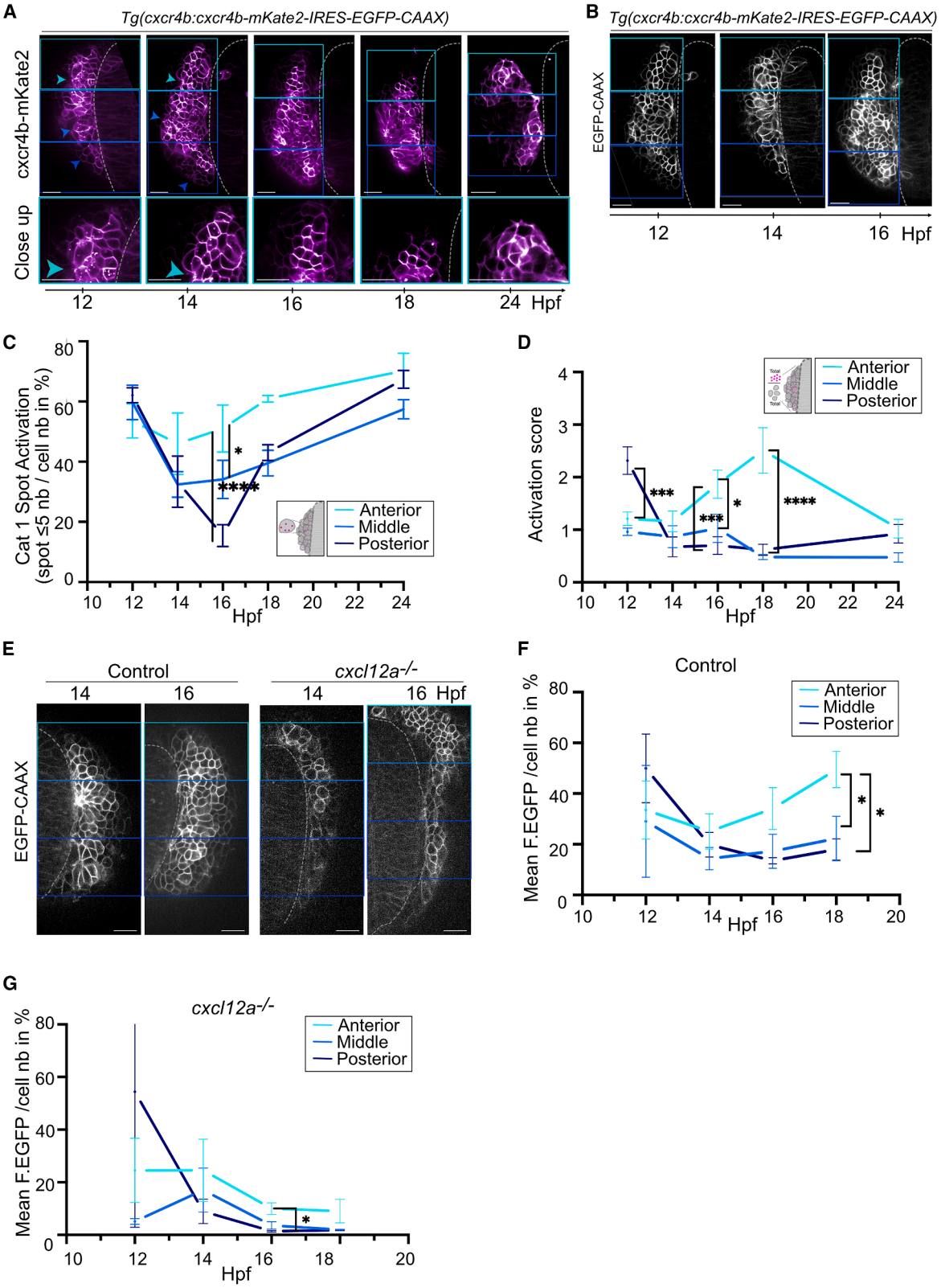

(legend on next page)

to 0.6 (±0.1, *n* = 4) at 18 hpf for cells in the posterior compartment (Figure 5D).

The specific response of the different compartments could be due to a specific distribution of Cxcr4b along the AP axis; the loss of function of *cxcl12a* could disrupt expression specifically in the anterior domain blocking the rescue of placode assembly by anterior expression of Cxcl12a in this area. To test this hypothesis, we analyzed the mean EGFP-CAAX fluorescence (F.EGFP) per cell expressing Cxcr4b in the different compartments in the control (Figures 5E and 5F) and *cxcl12a* mutant OP (Figures 5E and 5G). From 12 to 18 hpf, we found that the average fluorescence distribution follows the same dynamics as the activation score in control embryos (compare Figure 5D with 5F). Thus, cells in the anterior compartment have a higher overall average fluorescence than those in other compartments, increasing from 33.5 (±11.4, *n* = 4) at 12 hpf to 49.4 (±7.1 *n* = 4) at 18 hpf, whereas decreasing from 29 (±11, *n* = 4) at 12 hpf to 22.2 (±4.3, *n* = 4) at 18 hpf for cells in the middle compartment and from 49.8 (±13.5, *n* = 4) at 12 hpf to 17.9 (±4.2, *n* = 4) at 18 hpf for cells in the posterior compartment (Figure 5F).

Finally, we analyzed whether *cxcl12a* loss of function affected this distribution. Surprisingly, mutant placodes show the same Cxcr4b fluorescence per Cxcr4b-expressing cell profile as controls in the middle and posterior domains. Despite heterogeneity at 12 hpf, fluorescence decreased from 5 (±1, *n* = 12) at 12 hpf to 1.9 (±0.1, *n* = 5) at 18 hpf for cells in the middle compartment and from 54.4 (±51.5, *n* = 8) at 12 hpf to 1.8 (±0.1, *n* = 6) at 18 hpf for cells in the posterior compartment (Figure 5G). On the other hand, in the absence of *cxcl12a,* the distribution of this ratio in the anterior domain mirrors that of the other domains, with a decrease from 24.5 (±12.2, *n* = 8) at 12 hpf to 9 (±4.4, *n* = 7) at 18 hpf, revealing a specific effect on the distribution of Cxcr4b in the anterior domain.

The dynamics of the number of cells expressing Cxcr4b in the anterior compartment does not appear to be affected by the loss of function of *cxcl12a* (compare Figure S7A with Figure S8B). As described above, olfactory cells in the posterior and middle compartments show a similar Cxcr4b expression profile (i.e., an increase from 12 to 18 hpf followed by a slight decrease at 24 hpf, Figure S7A). In contrast, anterior olfactory cells saw their Cxcr4b expression levels decrease by half during the same period (Figure S7A). This trend is found again in mutant embryos, where the number of anterior cells decreases from 117.3 (±51.6, *n* = 12) at 12 hpf to 90.8 (±24.2, *n* = 8) at 18 hpf and from 187.833 (±50.7, *n* = 12) at 12 hpf to 183.2 (±56.6, *n* = 8) at 18 hpf for cells in the middle compartment, and from 156.2 (±53.9, *n* = 12) at 12 hpf to 200 (±48.6, *n* = 8) at 18 hpf for cells in the posterior compartment (Figure S8B). However, the overall number of cells is higher in all areas in the mutant condition, doubling in the anterior area at 12 hpf with 27.7 (±4.3, *n* = 4) in the control condition and 117.3 (±51.6, *n* = 12) in the mutant condition (Figures S7A and S8B). We compared the effect of Cxcl12a on the overall distribution of Cxcr4b expression. In control, the expression profile remains stable in the anterior region, with fluorescence decreasing slightly from 14.8 (±5.7, *n* = 4) at 12 hpf to 12.9 (±1, *n* = 4) at 18 hpf, and increasing in the other two compartments from 20.9 (±9.2, *n* = 4) at 12 hpf to 31.9 (±2.6, *n* = 4) at 18 hpf for cells in the middle compartment and from 14.1 (±5.6, *n* = 4) at 12 hpf to 21.6 (±1.4, *n* = 4) at 18 hpf for cells in the posterior compartment (Figure S8C). Surprisingly, this distribution is not affected by the loss of function of *cxcl12a* in the anterior compartment, where fluorescence remains stable, increasing from 4.2 (±0.1, *n* = 12) at 12 hpf to 4.6 (±0.1, *n* = 8) at 18 hpf. It is altered, however, in the other two compartments; it becomes stable in the posterior domain at 4.6 (±0.1, *n* = 12) at 12 hpf to 4.6 (±0.2, *n* = 8) at 18 hpf and increases slightly from 4.7 (±0.1, *n* = 12) at 12 hpf to 5.1 (±0.2, *n* = 4) at 18 hpf for cells in the middle compartment (Figure S8D).

Taken together, these results indicate that the anterior part of the OP has a limited number of cells capable of activating Cxcr4b relative to the middle and posterior compartments. However, activation of this pathway is maintained constant and receptor internalization is higher anteriorly than in other compartments during the early phases of olfactory cell compaction (from 12 to 16 hpf). During this period, our results indicate that Cxcr4b distribution is also modulated in the anterior-specific region, with expression increasing in a Cxcl12a-dependent manner (Figure 6).

Figure 5. The dynamics of Cxcl12a activation along the AP axis during olfactory placode assembly

(A and B) Left placode olfactory cells expressing (A) the Cxcr4b receptor, Cxcr4b-mKate2, and (B) their membranes, EGFP-CAAX, are visualized over time; blue arrowheads indicate the Cxcr4b+ spots. (A and B) An optical section is shown. The embryo is shown with the anterior up. Scale bars, 20 μm.

(C) Representation of the percentage of the mean number of intracellular Cxcr4b+ category 1 spots (i.e., percentage of the number of cells with between 1 and 5 Cxcr4b+ spots, relative to the total number of EGFP+ cells, see Figure S7A). At 16 hpf, a significant difference is observed between the anterior and middle domains, $^{*}p$ = 0.0171 (Cat1 spot activation is 51% ± 7.8% vs 34.1% ± 6.3%, *n* = 4 and 4, respectively) and between the anterior and posterior domains, $^{****}p < 0.0001$ (51% ± 7.8% vs 15.45% ± 3.6%, *n* = 4 and 4, respectively).

(D) Activation score of the Cxcl12a pathway (total number of Cxcr4b+ intracellular spots over the total number of EGFP+ cells) in anterior (light blue), middle (blue), and posterior (dark blue) cells as a function of time. The anterior domain shows a significantly lower activation score at 12 hpf than the posterior domain, $^{***}p$ = 0.0009 (1.2 ± 0.13 vs 2.3 ± 0.26, *n* = 4 and 4, respectively). This anterior score is then remarkably higher at 16 and 18 hpf compared with the other domains, middle: 16 hpf, $^{*}p$ = 0.0125 (1.9 ± 0.3 vs 1 ± 0.27, *n* = 4 and 4, respectively); 18 hpf, $^{****}p < 0.0001$ (2.5 ± 0.43 vs 0.5 ± 0.04, *n* = 4 and 4, respectively); and posterior: 16 hpf, $^{***}p$ = 0.0005 (1.9 ± 0.3 vs 0.7 ± 0.17, *n* = 4 and 4, respectively), 18 hpf, $^{****}p < 0.0001$ (2.5 ± 0.43 vs 0.6 ± 0.1, *n* = 4 and 4, respectively).

(E) Visualization of Cxcr4b expression in right placode olfactory cells over time in control and *cxcl12a*$^{-/-}$ embryos. A *z* projection is shown. The embryo is shown with the anterior up. Scale bars, 20 μm. Representation of the mean EGFP-CAAX fluorescence (F.EGFP) relative to the number of cells per domain (see Figure S8) in (F) control and (G) *cxcl12a*$^{-/-}$ embryos.

(F) The olfactory cells have an F.EGFP/cell number ratio that is globally higher than the other domains, particularly at 18 hpf, with a significant difference between the middle domain, $^{*}p$ = 0.0404 (49.4 ± 7.1 vs 22.25 ± 4.4, *n* = 4 and 4, respectively) and the posterior domain, $^{*}p$ = 0.0236 (49.4 ± 7.1 vs 17.94 ± 4.2, *n* = 4 and 4, respectively).

(G) This ratio fails to increase in the anterior domain from 14 to 18 hpf in *cxcl12a*$^{-/-}$ olfactory. However, it remains higher at 16 hpf in anterior cells compared with the posterior cells, $^{*}p$ = 0.0236 (9.9 ± 2.2 vs 1.4 ± 0.3, *n* = 4 and 4, respectively). Shown are mean ± SEM. *p* Values are calculated using a two-tailed t test.

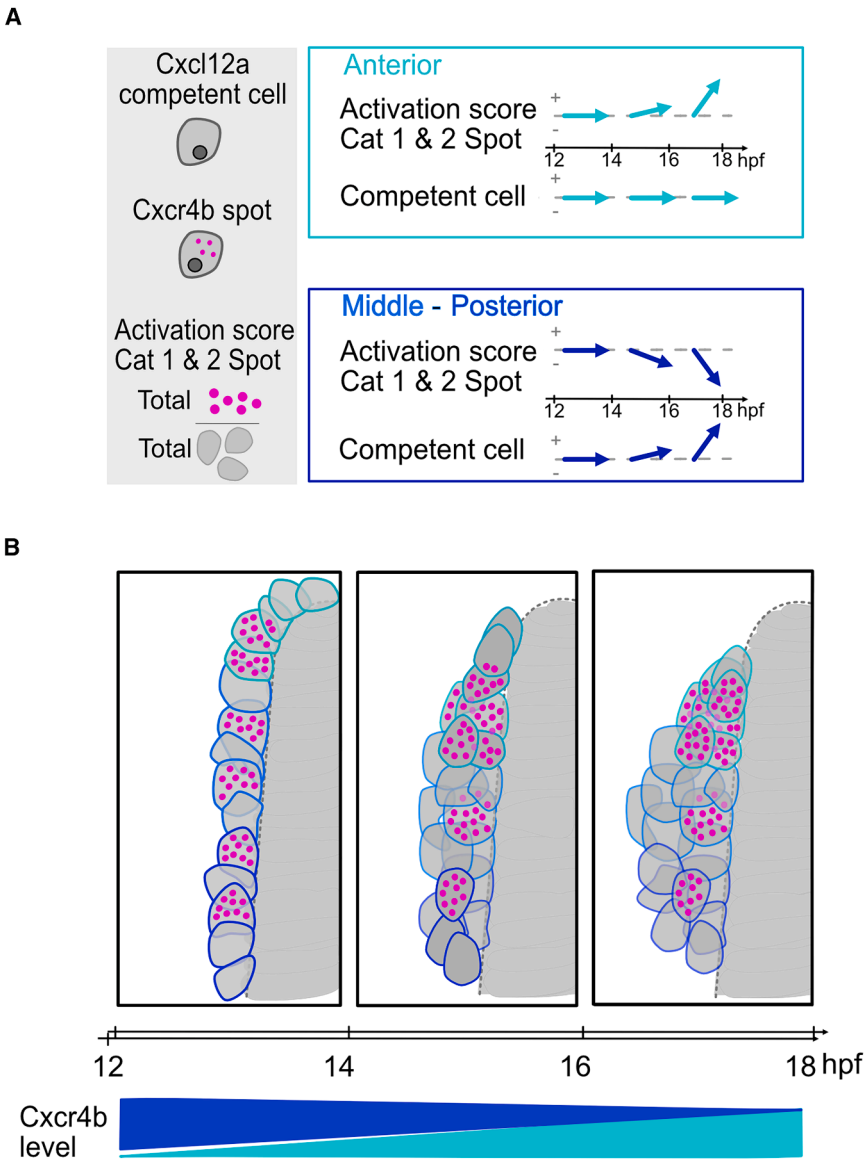

Figure 6. Schematic representation of the activation dynamics of Cxcl12a signaling

(A) Summary of the evolution of the parameters quantified in Figure 5 and S7 to analyze Cxcl12a signaling. Nuclei are shown in dark gray. Activation of Cxcl12a signaling is visualized by magenta circles representing Cxcr4b internalization in the cytoplasm (light gray). The anterior compartment is shown in light blue, whereas the middle-posterior compartments are shown in dark blue.

(B) Schematic of the dynamic evolution from 14 to 18 hpf of Cxcl12a signaling activation in a left olfactory placode during the compaction process.

DISCUSSION

Despite increasing knowledge concerning chemotaxis and the control of cell migration, how collectives of cells interpret chemotactic signals during organ formation is still underexplored. Here, we have employed mathematical simulations to help provide insights into this process, focusing on the zebrafish olfactory organ as a model.

We developed a simple mathematical framework to study zebrafish olfactory organ development based on only 4 parameters: chemoattraction, cell-cell interactions in the collective, cell-matrix interactions, and random cell motility. Actual values for the parameters of the model have not been measured. That said, the outcome of a lack of chemoattraction in the system is known as previous studies have shown that embryos mutant for the chemokine Cxcl12a or its receptor Cxcr4b display a characteristic defect in migration of precursor cells that will ultimately form the organ.[8,10] As such, we were able to set the first parameter of our model to 0 and adjust the relative values of those remaining to reproduce the phenotype reported in mutant zebrafish embryos. Our simulations indicated that in the absence of chemotaxis, the force represented by cell-cell interactions becomes the main driver of cell migration. Consistent with this observation, it has been shown in zebrafish that friction forces at the neuroectoderm-mesendoderm interface are generated by transient E-cadherin-mediated heterotypic contacts between different cell types,[29,30] reinforcing the idea that cell-cell interactions are central to morphogenesis processes.

With the model appropriately reproducing the *cxcl12a* mutant phenotype, we returned our focus to the chemoattraction parameter. Our simulations showed that cluster formation could be achieved by providing the chemoattractive signal at a variety of positions. Among the tested scenarios, however, only a simple gradient of signal from a restricted source induced cluster formation with cell kinetics comparable to those observed in embryos. If this reflects what is indeed happening in the embryo, it implies that the rates of diffusion and degradation of Cxcl12a are relatively constant and that precursor cells of the olfactory organ are competent to respond to the signal independently of their position along the AP axis. Also, and contrary to the broad transcription of *cxcl12a* throughout the anterior neural plate at early stages of development,[8,10] it suggests that the source of Cxcl12a protein is restricted within the anterior neural plate. This possibility is supported by the *in vivo* rescue of the *cxcl12a* mutant phenotype by IR-LEGO-induced restoration of Cxcl12a expression centrally in the anterior neural plate. An alternative hypothesis to explain our simulations would be that Cxcl12a is produced throughout the telencephalon, in keeping with the transcription

of the gene, and that an unknown mechanism in the precursor population would limit activation of the pathway. In the zebrafish posterior lateral line primordium, it has been shown that the interpretation of a uniform Cxcl12a stripe is achieved by the expression of two chemokine receptors, Cxcr4b and Ackr3b, whose localization is restricted within the migrating primordium.[26,31] To date, however, *ackr3b* expression has not been detected in EONs.

Testing the predictions of the mathematical model *in vivo*, we found that whereas posterior induction of Cxcl12a restored correct morphogenesis in *cxcl12a* mutants, anterior expression was unable to do so. To understand this discrepancy, we studied endogenous Cxcl12a signaling dynamics in live embryos using a pathway activation reporter.[26] Our data show that pathway activation displays a similar dynamics in the middle and posterior populations of OP precursors, with the number of olfactory cells competent to internalize Cxcl12a increasing over a period from 12 to 18 hpf. On the other hand, a general decrease in activation is detected in the anterior compartment during this time window, and a small population of anterior precursors maintains high Cxcr4b internalization. Whether these differences underlie those observed between our simulations and IR-LEGO rescue experiments remains to be seen. Unfortunately, it is not possible to determine if anterior IR-LEGO is able to induce a population of cells internalizing high levels of Cxcr4b given the genetic tools available. Nonetheless, it will be interesting to determine if the migratory behavior of this population of anterior precursor cells differs from others in the anterior compartment. As predicted by the interplay between our model and *in vivo* experiments, activation of the pathway appears to be modulated within OP precursors along the AP axis.

Our results show that Cxcl12a specifically regulates Cxcr4b in anterior olfactory cells between 14 and 18 hpf. This suggests a positive feedback mechanism allowing specific expression of Cxcr4b anteriorly to generate constant activation by Cxcl12a in the anterior domain that would allow both migration of olfactory cells toward the posterior and a retention of anterior cells around the telencephalon, resisting the overall anterior movement of cells/tissues during embryonic growth.[1] It would be interesting to analyze this feedback at the molecular level and determine whether Cxcl12a controls the expression of Cxcr4b transcriptionally or translationally.

It has been shown that OP derivatives are structured by different levels of expression of the distal-less (dlx) gene, which subdivide the anterior neuroectoderm into OP precursors (high Dlx expression) and olfactory bulb precursors (lower Dlx expression). Interestingly, at 16 hpf, cells located in the most anterior region of the OP domain are positive for both Dlx3b and Six4b. In contrast, cells located in the more posterior region of the OP domain are positive for Dlx3b, revealing the heterogeneity of olfactory cells along the AP axis.[32,33] Notably, Six4 also modulates regulates Cxcr4b-dependent chemosensitivity in skin cancers.[34] It is thus tempting to hypothesize that Six4b could regulate Cxcl12a-Cxcr4b signaling in anterior olfactory cells to control placode assembly.

Limitations of the study

Despite the interesting insights we have gained confronting a theoretical framework and *in vivo* experiments, our study has limitations. First, our mathematical model is extremely simplified. We could have tried to take other parameters such as cell proliferation and apoptosis into account. However, during the period of interest, there are few mitoses and the described wave of apoptosis only starts at 24 hpf.[6] Second, in this model, we analyzed the distribution of the source in the telencephalon, whereas hindsight suggests that it will be crucial to understand how olfactory cells perceive the Cxcl12a signal. Third, our model does not take into account the evolution of the relationship between cells. A "neighborhood watch" model has been employed to explain the formation of the primitive streak in the chicken embryo because embryonic epiblast cells evaluate positional information relative to their neighbors.[35] We based our approach on a region-based view of the dynamics of Cxcl12a signaling given by our previous work,[10] but our model lacks an *in vivo* cellular scale. Knowing how the dynamics of Cxcl12a signaling evolves at the cellular scale would give us a better understanding of how cells integrate this signaling in relationship to each other. Finally, our model treats our 4 parameters as independent, whereas there are potential links between them, in particular between Cxcl12a signaling and Cell-Cell or Cell-Matrix interactions. Indeed, in the lateral line, all the cells of the primordium must detect the attractant and adhere to each other to coordinate their movements and display a robust directed migration.[36] This suggests that a more complex, probably multi-scale model will need to be developed in the future to explore the spatial and temporal heterogeneity of Cxcl12a signaling and cell activation further.

RESOURCE AVAILABILITY

Lead contact

Further information and requests for resources and reagents should be directed to and will be fulfilled by the lead contact, Julie Batut (julie.batut@utoulouse.fr).

Materials availability

Transgenic zebrafish lines and plasmids generated in this study will be shared by the lead contact upon request. Embryo 4D datasets were generated for this study with a total of six wild-type embryos and five mutant embryos. Datasets can be downloaded from the BioEmergences database upon request and have been deposited in Mendeley. DOIs are listed in the key resources table.

Digital lineages were generated for this study with a total of six wild-type embryos and five mutant embryos. Lineages can be downloaded through the BioEmergences software tool Mov-It and have been deposited in Mendeley. DOIs are listed in the key resources table.

Simulation descriptors and Biomechanical maps were generated for this study. They can be readily computed using the code over the cell lineage.

Data and code availability

- Data: The published article includes all datasets and codes generated during this study. Raw trajectories, tracks, meantracks, and AP Length used to make the figures can be found in the GitHub repository: https://github.com/JulieBatut/Zilliox-Letort_2024.git. Raw microscopy images generated in this paper will be shared by the lead contact upon request.
- Code: All custom code for the mathematical modeling and the specific parameters for each figures are available on github: https://github.com/gletort/Morphoe, and https://github.com/JulieBatut/Zilliox-Letort_2024. Simulations of trajectories were generated for this study. They can be easily reproduced using the code available in the GitHub repository. microscopy analyses have been deposited on Github at https://github.com/JulieBatut/Zilliox-Letort_2024.

- Other items: Any additional information required to reanalyze the data reported in this work paper is available from the lead contact upon request.

ACKNOWLEDGMENTS

This work was supported by the Centre National de la Recherche Scientifique (CNRS) as part of its *Biomimetisme* interdisciplinary program over the 2019–2020 period, Université de Toulouse III (UPS), the Ministère de la Recherche, and the *Agence Nationale de la Recherche* (ANR), with the ZOORRO grant, ANR-23-CE45-0021. We thank Holger Knaut, Darren Gilmour, Kristen Kwan, and Chi-Bin Chien for providing plasmids; Stéphanie Bosch; Brice Roncin; Vanessa Dougados; Thomas Mangeat and the Toulouse RIO Imaging platform; and zootechnicians for taking care of the fish. We also thank EMBO Workshop MMM2017 and members of the Batut lab for advice and comments on the manuscript.

AUTHOR CONTRIBUTIONS

Conceptualization, J.B; methodology, M.Z., G.L., P.D., A.P., D.S., and J.B.; investigation, M.Z., G.L., P.B., V.R.-M., D.S., and J.B.; visualization, C.R., M. Z., G.L., D.S., M.Z., and J.B.; supervision, D.S., P.B., and J.B.; writing – original draft, J.B., M.Z., and G.L.; writing – review & editing, M.Z., G.L., F.G.-I., P.B., D. S., and J.B.

DECLARATION OF INTERESTS

The authors declare no competing financial interests.

STAR★METHODS

Detailed methods are provided in the online version of this paper and include the following:

- KEY RESOURCES TABLE
- EXPERIMENTAL MODEL AND STUDY PARTICIPANT DETAILS
- METHOD DETAILS
  - Model (https://github.com/JulieBatut/Zilliox-Letort_2024.git)
  - Cell description
  - Cell-cell interactions (a)
  - Chemotaxis (b)
  - Cell-matrix interaction (c)
  - Cell motility (d)
- QUANTIFICATION AND STATISTICAL ANALYSIS

SUPPLEMENTAL INFORMATION

Supplemental information can be found online at https://doi.org/10.1016/j.isci.2025.113398.

Received: January 16, 2025
Revised: June 22, 2025
Accepted: August 15, 2025
Published: August 19, 2025

REFERENCES

1. Aguillon, R., Blader, P., and Batut, J. (2016). Patterning, morphogenesis, and neurogenesis of zebrafish cranial sensory placodes. Methods Cell Biol. *134*, 33–67.
2. Francis-West, P.H., Ladher, R.K., and Schoenwolf, G.C. (2002). Development of the sensory organs. Sci. Prog. *85*, 151–173.
3. Whitlock, K.E. (2015). The loss of scents: do defects in olfactory sensory neuron development underlie human disease? Birth Defects Res. C Embryo Today. *105*, 114–125.
4. Miyasaka, N., Wanner, A.A., Li, J., Mack-Bucher, J., Genoud, C., Yoshihara, Y., and Friedrich, R.W. (2013). Functional development of the olfactory system in zebrafish. Mech. Dev. *130*, 336–346.
5. Whitlock, K.E. (2008). Developing a sense of scents: Plasticity in olfactory placode formation. Brain Res. Bull. *75*, 340–347, . Preprint at. https://doi.org/10.1016/j.brainresbull.2007.10.054.
6. Whitlock, K.E., and Westerfield, M. (2000). The olfactory placodes of the zebrafish form by convergence of cellular fields at the edge of the neural plate. Development (Cambridge, England) *127*, 3645–3653.
7. Breau, M.A., Bonnet, I., Stoufflet, J., Xie, J., De Castro, S., and Schneider-Maunoury, S. (2017). Extrinsic mechanical forces mediate retrograde axon extension in a developing neuronal circuit. Nat. Commun. *8*, 282.
8. Miyasaka, N., Knaut, H., and Yoshihara, Y. (2007). Cxcl12/Cxcr4 chemokine signaling is required for placode assembly and sensory axon pathfinding in the zebrafish olfactory system. Development *134*, 2459–2468.
9. Madelaine, R., Garric, L., and Blader, P. (2011). Partially redundant proneural function reveals the importance of timing during zebrafish olfactory neurogenesis. Development *138*, 4753–4762.
10. Aguillon, R., Madelaine, R., Aguirrebengoa, M., Guturu, H., Link, S., Dufourcq, P., Lecaudey, V., Bejerano, G., Blader, P., and Batut, J. (2020). Morphogenesis is transcriptionally coupled to neurogenesis during peripheral olfactory organ development. Development (Camb.) *147*, dev192971.
11. Sharpe, J. (2017). Computer modeling in developmental biology: growing today, essential tomorrow. Development (Cambridge, England) *144*, 4214–4225.
12. Zilliox, M., Tillement, V., Mangeat, T., Polès, S., Blader, P., and Batut, J. (2023). Protocol to locally express cxcl12a during zebrafish olfactory organ development by combining IR-LEGO with live imaging. STAR Protoc. *4*, 102538.
13. Barnhart, E.L., Allard, J., Lou, S.S., Theriot, J.A., and Mogilner, A. (2017). Adhesion-Dependent Wave Generation in Crawling Cells. Curr. Biol. *27*, 27–38.
14. Camley, B.A., and Rappel, W.-J. (2017). Physical models of collective cell motility: from cell to tissue. J. Phys. D Appl. Phys. *50*, 113002.
15. Hakim, V., and Silberzan, P. (2017). Collective cell migration: a physics perspective. Rep. Prog. Phys. *80*, 076601.
16. Méhes, E., and Vicsek, T. (2014). Collective motion of cells: from experiments to models. Integr. Biol. *6*, 831–854.
17. Simsek, M.F., and Özbudak, E.M. (2022). Patterning principles of morphogen gradients. Open Biol. *12*, 220224.
18. Szabó, B., Szöllösi, G.J., Gönci, B., Jurányi, Z., Selmeczi, D., and Vicsek, T. (2006). Phase transition in the collective migration of tissue cells: Experiment and model. Phys. Rev. E - Stat. Nonlinear Soft Matter Phys. *74*, 061908. https://doi.org/10.1103/PhysRevE.74.061908.
19. Monnot, P., Gangatharan, G., Baraban, M., Pottin, K., Cabrera, M., Bonnet, I., and Breau, M.A. (2022). Intertissue mechanical interactions shape the olfactory circuit in zebrafish. EMBO Rep. *23*, e52963.
20. Knutsdottir, H., Zmurchok, C., Bhaskar, D., Palsson, E., Dalle Nogare, D., Chitnis, A.B., and Edelstein-Keshet, L. (2017). Polarization and migration in the zebrafish posterior lateral line system. PLoS Comput. Biol. *13*, e1005451.
21. Streichan, S.J., Valentin, G., Gilmour, D., and Hufnagel, L. (2011). Collective cell migration guided by dynamically maintained gradients. Phys. Biol. *8*, 045004.
22. Friedrich, B.M., and Jülicher, F. (2009). Steering Chiral Swimmers along Noisy Helical Paths. Phys. Rev. Lett. *103*, 068102.
23. Painter, K.J. (2009). Continuous models for cell migration in tissues and applications to cell sorting via differential chemotaxis. Bull. Math. Biol. *71*, 1117–1147.
24. Deguchi, T., Itoh, M., Urawa, H., Matsumoto, T., Nakayama, S., Kawasaki, T., Kitano, T., Oda, S., Mitani, H., Takahashi, T., et al. (2009). Infrared

laser-mediated local gene induction in medaka, zebrafish and Arabidopsis thaliana. Dev. Growth Differ. *51*, 769–775.

25. Wong, M., Newton, L.R., Hartmann, J., Hennrich, M.L., Wachsmuth, M., Ronchi, P., Guzmán-Herrera, A., Schwab, Y., Gavin, A.C., and Gilmour, D. (2020). Dynamic Buffering of Extracellular Chemokine by a Dedicated Scavenger Pathway Enables Robust Adaptation during Directed Tissue Migration. Dev. Cell *52*, 492–508.e10.
26. Venkiteswaran, G., Lewellis, S.W., Wang, J., Reynolds, E., Nicholson, C., and Knaut, H. (2013). Generation and Dynamics of an Endogenous, Self-Generated Signaling Gradient across a Migrating Tissue. Cell *155*, 674–687.
27. Schindelin, J., Arganda-Carreras, I., Frise, E., Kaynig, V., Longair, M., Pietzsch, T., Preibisch, S., Rueden, C., Saalfeld, S., Schmid, B., et al. (2012). Fiji: an open-source platform for biological-image analysis. Nat. Methods *9*, 676–682.
28. Stringer, C., Wang, T., Michaelos, M., and Pachitariu, M. (2021). Cellpose: a generalist algorithm for cellular segmentation. Nat. Methods *18*, 100–106.
29. Smutny, M., Ákos, Z., Grigolon, S., Shamipour, S., Ruprecht, V., Čapek, D., Behrndt, M., Papusheva, E., Tada, M., Hof, B., et al. (2017). Friction forces position the neural anlage. Nat. Cell Biol. *19*, 306–317.
30. Messer, C.L., and McDonald, J.A. (2023). Expect the unexpected: conventional and unconventional roles for cadherins in collective cell migration. Biochem. Soc. Trans. *51*, 1495–1504.
31. Donà, E., Barry, J.D., Valentin, G., Quirin, C., Khmelinskii, A., Kunze, A., Durdu, S., Newton, L.R., Fernandez-Minan, A., Huber, W., et al. (2013). Directional tissue migration through a self-generated chemokine gradient. Nature *503*, 285–289.
32. Torres-Paz, J., Tine, E.M., and Whitlock, K.E. (2021). Dissecting the neural divide: a continuous neurectoderm gives rise to the olfactory placode and bulb. Int. J. Dev. Biol. *65*, 275–287.
33. Harden, M.V., Pereiro, L., Ramialison, M., Wittbrodt, J., Prasad, M.K., McCallion, A.S., and Whitlock, K.E. (2012). Close association of olfactory placode precursors and cranial neural crest cells does not predestine cell mixing. Dev. Dyn. *241*, 1143–1154.
34. Vazirabad, A.F., Noorolyai, S., Baghbani, E., Mahboob, S., Zargari, F., Rahmani, S., Sorkhabi, A., Montazami, N., Sameti, P., and Baradaran, B. (2022). Silencing of SiX-4 enhances the chemosensitivity of melanoma cells to Cisplatin. Pathol. Res. Pract. *240*, 154194.
35. Lee, H.C., Hastings, C., Oliveira, N.M.M., Pérez-Carrasco, R., Page, K.M., Wolpert, L., and Stern, C.D. (2022). Neighbourhood watch' model: embryonic epiblast cells assess positional information in relation to their neighbours. Development *149*, dev200295.
36. Colak-Champollion, T., Lan, L., Jadhav, A.R., Yamaguchi, N., Venkiteswaran, G., Patel, H., Cammer, M., Meier-Schellersheim, M., and Knaut, H. (2019). Cadherin-Mediated Cell Coupling Coordinates Chemokine Sensing across Collectively Migrating Cells. Curr. Biol. *29*, 2570–2579.e7.
37. Haas, P., and Gilmour, D. (2006). Chemokine Signaling Mediates Self-Organizing Tissue Migration in the Zebrafish Lateral Line. Dev. Cell *10*, 673–680.
38. Blader, P., Plessy, C., and Strähle, U. (2003). Multiple regulatory elements with spatially and temporally distinct activities control neurogenin1 expression in primary neurons of the zebrafish embryo. Mech. Dev. *120*, 211–218.
39. Valentin, G., Haas, P., and Gilmour, D. (2007). The Chemokine SDF1a Coordinates Tissue Migration through the Spatially Restricted$\sim$Activation$\sim$of Cxcr7 and Cxcr4b. Curr. Biology *17*.
40. Sundaramoorthy, E., Leonard, M., Mak, R., Liao, J., Fulzele, A., and Bennett, E.J. (2017). ZNF598 and RACK1 Regulate Mammalian Ribosome-Associated Quality Control Function by Mediating Regulatory 40S Ribosomal Ubiquitylation. Mol. Cell *65*, 751–760.e4.
41. Kimmel, C.B., Ballard, W.W., Kimmel, S.R., Ullmann, B., and Schilling, T.F. (1995). Stages of embryonic development of the zebrafish. Dev. Dyn. *203*, 253–310.
42. An, G., Mi, Q., Dutta-Moscato, J., and Vodovotz, Y. (2009). Agent-based models in translational systems biology. Wiley Interdiscip. Rev. Syst. Biol. Med. *1*, 159–171.
43. Letort, G., Montagud, A., Stoll, G., Heiland, R., Barillot, E., Macklin, P., Zinovyev, A., and Calzone, L. (2019). PhysiBoSS: a multi-scale agent-based modelling framework integrating physical dimension and cell signalling. Bioinformatics (Oxford, England) *35*, 1188–1196.
44. Camley, B.A., Zimmermann, J., Levine, H., and Rappel, W.-J. (2016). Emergent Collective Chemotaxis without Single-Cell Gradient Sensing. Phys. Rev. Lett. *116*, 098101.
45. Osborne, J.M., Fletcher, A.G., Pitt-Francis, J.M., Maini, P.K., and Gavaghan, D.J. (2017). Comparing individual-based approaches to modelling the self-organization of multicellular tissues. PLoS Comput. Biol. *13*, e1005387.
46. Sepúlveda, N., Petitjean, L., Cochet, O., Grasland-Mongrain, E., Silberzan, P., and Hakim, V. (2013). Collective cell motion in an epithelial sheet can be quantitatively described by a stochastic interacting particle model. PLoS Comput. Biol. *9*, e1002944.
47. Van Liedekerke, P., Palm, M.M., Jagiella, N., and Drasdo, D. (2015). Simulating tissue mechanics with agent-based models : concepts, perspectives and some novel results. COMPUTATIONAL PARTICLE MECHANICS *2*, 401–444.

STAR★METHODS

KEY RESOURCES TABLE

REAGENT or RESOURCE	SOURCE	IDENTIFIER
Experimental models: Organisms/strains		
Zebrafish: *Tg(hsp70l:mCherry-cxcl12a)*^{zf331225}: zf3312Tg	Wong et al.[25]	ZFIN: ZDB-ALT-211116-7
Zebrafish: *Tg(-8.0cldnb:lynGFP)*^{zf106}: zf106Tg	Haas and Gilmour[37]	ZFIN: ZDB-ALT-060919-2
Zebrafish: *TgBAC(cxcr4b:cxcr4b-mKate2-IRES-EGFP-CAAX,cryaa:DsRed)*^{sk79}: sk79Tg	Venkiteswaran et al.[26]	ZFIN: ZDB-ALT-140205-5
Zebrafish: *Tg(-8.4neurog1:gfp)*^{sb1} sb1Tg	Blader et al.[38]	ZDB-ALT-030904-6
Zebrafish: cxcl12a^{t30516}: t30516	Valentin et al.[39]	ZDB-FISH-150901-11306
Chemicals, peptides, and recombinant proteins		
Petri Dish 90 × 16.2 mm	Dutcher	Cat#688307
Low melting Agarose	Sigma	Cat#15568025
35 mm dish, High precision 1.5 coverslip 14 mm glass diameter	MATTEK	Cat#P35G-0.170-14-C
Software and algorithms		
Metamorph (Version 7.10.5.476)	Leica	Cat#8106710
ROE SysCon (Version 1.1.6.9)	Rapp OptoElectronic GmbH	Cat#ROE SysCon Software
Fiji	Fiji/imageJ2 open source	https://imagej.net/software/fiji/
Imaris 8.3	Oxford Instruments	https://imaris.oxinst.com/
Image analysis	This paper	https://github.com/JulieBatut/Zilliox-Letort_2024.git
Mathematical Modeling	This paper	https://github.com/gletort/Morphoe
Other		
Dumont#5 Forceps – 0.08 × 0.004 mm – Carbon Steel	Fine Science Tools	Cat#11251-10
Heat block Stuart SBH130DC Model	Dutscher	Cat#001184
Spinning disk - Leica inverted DMi8 microscope	Leica	Cat#11889113
Andor-CSUX1-M1*N*-5000-4L Spinning disk YOKOGAWA CSUX1 M1N1 5000 –rotative disk Nipkow	Leica	Cat#8110529
Fast SCMOS camera (ORCA FLASH4 V2+ Hamamatsu)	Leica	Cat#8110774
Objective HCX PL APO, 40x NA 1.3, WD 0.22	Leica	Cat#11506329
Super Z galvanometric stage (250 µm) for DMi8	Leica	Cat#11640260
IR-LEGO Setup	Rapp OptoElectronic GmbH	Cat#UGA-42 Geo
DL-1470/1000 Diode Laser System Wavelength: 1470 nm/Power:1.0 W	Rapp OptoElectronic GmbH	Cat#DL-1470
Objective HC PL IRAPO 40x/1.10 W CORR	Leica	Cat#15506352
Calibration sample: Phosphor Micro Upconverting Particles	Rapp OptoElectronic GmbH[40]	https://doi.org/10.1021/acsami.6b15322

EXPERIMENTAL MODEL AND STUDY PARTICIPANT DETAILS

Ethics Statement and Embryos: All zebrafish and embryos were handled according to relevant national and international guidelines. French veterinary services and the local ethical committee approved the protocols used in this study, with approval ID: E31555011 and APAPHIS #34368-2021121409357964-v6. The laboratory (CBI FR 3743) has all the necessary authorizations to house and work with transgenic and mutant zebrafish strains. All work carried out with zebrafish has been strictly in accordance with the European Animal Protection Directive (2010/63/EU), the European Convention for the Protection of Vertebrate Animals, and national and local legislation. The staff responsible for fish breeding has undergone specific training on these issues. The fish facility complied with all national and European laws and regulations relating to the transport, housing and use of fish in research, and the fish populations were kept in approved tanks. Approved veterinarians regularly check the health status of the facility and the fish being bred, and are responsible for ensuring compliance with all regulations and the implementation of all necessary animal welfare provisions. All experimental procedures, the killing of fish embryos after experiments and the disposal of embryos were carried out in accordance with all national and European laws and regulations. Fish were maintained at the CBI zebrafish facility in accordance with the rules and protocols in place. Transgenic zebrafish lines carrying a gene construct for the expression of a fluorescent protein were used for this study. The list is detailed in the Key resource table. Embryos were obtained through natural crosses and staged according to.[41] All embryos were obtained from natural crosses and processed up to imaging as described previously.[12] They were imaged using a dorsal view, and the imaged field included the forebrain and olfactory placodal cells, with some differences depending on the position of the embryo in its agarose mold. With regard to sex, the embryos were imaged at an early stage that did not allow for the identification of males and females.

METHOD DETAILS

Model (https://github.com/JulieBatut/Zilliox-Letort_2024.git)

To explore numerically the formation of the olfactory placode, we modeled the motion of cells at the individual cell level and used an agent-based approach.[42] For simplicity, cells were considered identical and represented as circles of constant radius that can move and interact. Similar off-lattice particle/cell-centered models were indeed used to simulate multi-cellular cell systems and collective motion.[43–47] Each cell i was represented by the position of its center p_i. Under the standard assumption of low Reynolds number regime, the equation of motion for each cell center was $\frac{d\overrightarrow{p_i}}{dt} = \overrightarrow{F_{tot,i}}$.

In our model, we considered that the motion of the cells was determined by 4 main factors: the interaction with its neighbors (a), the attraction from the chemotaxis source (b), the interaction with the extra-cellular matrix (telencephalon) (c) and the spontaneous motility of an individual cell (d). Thus, the displacement of one cell i was calculated as:

$$d\overrightarrow{p}_i = \underbrace{\sum_{j\neq i}\overrightarrow{F}_{ij}dt}_{(a)} + \underbrace{\overrightarrow{F}_{i,chem}dt}_{(b)} + \underbrace{\overrightarrow{F}_{i,ecm}dt}_{(c)} + \underbrace{\overrightarrow{\eta}_i}_{(d)} \quad \text{(Equation 1)}$$

$\overrightarrow{p}_i = (x_i, y_i)$ is the position of the center of the cell i at time t.

Cell description

For simplification, we described an individual cell as a circle of radius $d_{eq}/2$, equal for all cells. However, the cells could interact with each other until a distance d_{lim} greater than d_{eq} to take into account the presence of protrusions in the cells (like filopodia).

Cell-cell interactions (a)

When 2 cells are within a distance smaller than d_{lim} from each other, their contact will influence their motion. At first, close cells which do not overlap will attract each other by forming junctions upon contact, which permits cells clustering. However, as the cell cannot physically overlap, if the distance between their center decreases below the equilibrium distance d_{eq} then there will be a hard-core repulsion to account for the limited deformability of the cells.

The force applied on one cell i by its neighboring cell j is then calculated as:

$$\overrightarrow{F_{ij}} = c_{ij}\text{inter}\left(\overrightarrow{p_j} - \overrightarrow{p_i}\right)$$

where

$$\text{inter} = \begin{cases} \dfrac{d_{ij} - d_{eq}}{d_{ij}} & if\, d_{ij} > d_{eq}, \\ -\left(\dfrac{d_{ij} - d_{eq}}{d_{ij}}\right)^2 & if\, d_{ij} \leq d_{eq}. \end{cases} \quad \text{(Equation 2)}$$

Chemotaxis (b)

We wanted to test the contribution of a chemotaxis agent present in the middle of the telencephalon. Thus, we added a force attracting the cells toward the point source of coordinates (0,0). We tested two scenarios. In the first one we assume that this attraction depends on the distance of the cell to this point source (Equation 3_dist), and increase as the cell got closer to this point (the cell receives more signal as the cell gets closer to the source). In the second case, the attraction follows a constant gradient (Equation 3_const) and is thus independent from the distance to the source.

$$\vec{F}_{i,chem,dist} = \frac{\text{chem}}{1+\|\vec{p}_i\|}\frac{-\vec{p}_i}{\|\vec{p}_i\|} \quad \text{(Equation 3_dist)}$$

$$\vec{F}_{i,chem,const} = \text{chem}'\frac{-\vec{p}_i}{\|\vec{p}_i\|} \quad \text{(Equation 3_const)}$$

where chem and chem′ are the strengths of the attraction force in the different cases.

Cell-matrix interaction (c)

For simplicity, the matrix (telencephalon) was implemented with a parabolic shape, which was sufficient to roughly resemble biological shape. As for the cell-cell interaction, we considered in the model the effect of the interaction between each cell and the matrix. Cells tend to adhere to the matrix which is represented in the model by an attractive force, but cannot cross it, which is calculated as repulsive force between the matrix and the cell. This interaction is thus calculated as:

$$\vec{F}_{i,ecm} = \text{ecm}\left(\|\vec{p}_{ecm}-\vec{p}_i\| - \frac{d_{eq}}{2}\right)\frac{\left(\vec{p}_{ecm}-\vec{p}_i\right)}{\|\vec{p}_{ecm}-\vec{p}_i\|} \quad \text{(Equation 4)}$$

Where ecm is the strength of the attractive/repulsive forces between one cell and the matrix, and $\vec{p}_{ecm}$ is the closest point of the matrix to the cell (projected point) where the interaction is considered to take place. For numerical reason, we increased the repulsion coefficient if the cell got inside the matrix $\vec{F}_{i,ecm} = 100(\vec{p}_{ecm}-\vec{p}_i)$ to ensure that the cells stay outside.

Cell motility (d)

The goal of the model is to test the effect of the different forces on the cell motility, taking into account only essential components. Thus, we simplified the description of the cell motility as a random Brownian motion:

$$\vec{\eta}_i(t) = \sqrt{2D}dB_t, \quad \text{(Equation 5)}$$

Note that we also tested a model in which we took into account the polarized motion of the cell by keeping a persistence of direction (due to the internal organization of the cell), and that did not impact the general behavior.

N	60
dt	0.0005
tmax	6
dlim	1
deq	0.5
Chem	2
D	0.001
v0	0.1
cij	0.7
ecm	4

All the parameters for each simulation are shown here: https://github.com/JulieBatut/Zilliox-Letort_2024. The source code for the simulations, developed in python are publicly available here: https://github.com/gletort/Morphoe/tree/main.

IR-LEGO and time-lapse spinning disk datasets

Embryos carrying both *Tg(-8.0cldnb:lynGFP)*^{zf106} and *Tg(hsp:mcherry-cxcl12a)* transgenes and control or mutant for *cxcl12a*^{t30516} were selected. Embryos were then grown to 12 hpf at which point they were dechorionated and embedded for imaging in 0.7%

low-melting point agarose in embryos medium. For Infra-Red (IR) LEGO, a 40x HC PL IRAPO/1.10 W CORR lens (Leica, 15506352) was used to perform 90% IR 1470 nm laser illumination for 1min over a 22 μm radius in the middle, anterior or posterior of the telencephalon depending on the experiment. This illumination was performed using the in-house IR-LEGO configuration[12] and a time-lapse series of confocal stacks (0.7 μm slice/100 μm deep) was generated of the anterior neural plate and flanking non-neural ectoderm on an inverted Leica DMi8 Spinning microscope using a 40x HC PL APO/1.3 oil objective (Leica, 11506329). Acquisitions each 1 h were stopped at 24 hpf (t^{final}), when the olfactory rosette was clearly visible. The shape of the olfactory rosette was then defined using Imaris 8.3 analysis software (Bitplane, Switzerland). IR-LEGO and Imaging data have been collected by Rapp'Opto software and Metamorph software (version: Metamorph 7.8.13.0) respectively.

In vivo *imaging: Cxcl12a dynamic data collection and processing*

Embryos carrying *Tg(cxcr4b:cxcr4b-mKate2-IRES-EGFP-CAAX)* transgene were selected. Embryos were then grown to 12 hpf at which point they were dechorionated and embedded for imaging in 0.7% low-melting point agarose in embryos medium. A time-lapse series of confocal stacks (0.3 μm slice/120 μm deep) was generated of the anterior neural plate and flanking non-neural ectoderm on an inverted Leica DMi8 Spinning microscope using a 40x HC PL APO/1.3 oil objective (Leica, 11506329). Acquisitions each 1 h were stopped at 24 hpf (t^{final}), when the olfactory rosette was clearly visible. A Fiji macro has been developed to analyze Cxcl12a activation in olfactory cells. Briefly, after selection and (anisotropic) filtering of the red (561, Cxcr4b-mKate2) and green (EGFP-CAAX) images, the pools of cells with a green membrane were segmented and extracted using cellpose 2.0 (https://www.cellpose.org/). Finally, a macro to quantify the number of red clusters and their intensities (reflecting Cxcl12a activation by Cxcr4b) was generated. All the data for this quantification are available on github (https://github.com/JulieBatut/Zilliox-Letort_2024.git).

QUANTIFICATION AND STATISTICAL ANALYSIS

All statistical comparisons are indicated in figure legends including one sample and paired t-test performed using Prism (GraphPad.) The scatter dot plots were generated with Prism. Data are mean ± s.e.m. Two-tailed t-test $^{ns}p > 0.05$, $^{*}p < 0.05$, $^{**}p < 0.01$, $^{***}p < 0.001$, $^{****}p < 0.0001$.